Iranian Journal of Medical Physics

ijmp.mums.ac.ir

# Assessment of Neutron Contamination in Small Fields of Elekta Synergy Linac in High Energy Photon Beams

Zahra Poshtekeshi[1], Abbas Haghparast[1], Mahdi Ghorbani[2*], Hedieh Ranji[2], Meysam Tavakoli[3]

1. Department of Medical Physics, Faculty of Medicine, Kermanshah University of Medical Sciences, Kermanshah, Iran
2. Biomedical Engineering and Medical Physics Department, School of Medicine, Shahid Beheshti University of Medical Sciences, Tehran, Iran
3. Department of Radiation Oncology, Winship Cancer Institute, Emory University, Atlanta, GA, United States of America.

**ARTICLE INFO**

***Article type:***
Original Paper

***Keywords:***
Radiotherapy
Medical Linear Accelerator
Neutron Contamination
CR-39
Small Field
Elekta Synergy

**ABSTRACT**

***Introduction:*** Since technique such as intensity-modulated radiation therapy (IMRT) and Volumetric Modulated Arc Therapy (VMAT) use small fields (< 5 × 5 cm²), data on neutron contamination in such conditions remain limited. This study evaluated neutron dose equivalent (NDE) levels in small fields in 10 MV and 18 MV photon beam energies for Elekta synergy linac.

***Material and Methods:*** Fast NDE were measured by using CR-39 detectors, calibrated with a $^{241}$Am-Be neutron source. Measurements were conducted at five field sizes (1 × 1 to 5 × 5 cm²) in both 10 MV and 18 MV energies, at the isocenter that was aligned with the center of the field, 5 cm and 10 cm distances from the field edge, and at $d_{max}$ in a SP34 solid water phantom (Scanditronix-Welhofer, Germany).

***Results:*** The highest NDE (8.18 mSv/Gy) occurred at the isocenter (center of the field) for a 1 × 1 cm² field in 18 MV- five times higher than that for a 5 × 5 cm² field. NDE at $d_{max}$ was lower by ~88% at the center of the field, and by ~90% at 10 cm from the field edge compared to the center of the field for a 1 × 1 cm² field in 18 MV energy.

***Conclusion:*** NDE increased with decreasing field sizes, at 10 MV and 18 MV energies. This effect should be considered in treatment planning for techniques that use small fields, due to its potential biological risks.

►*Please cite this article as:*
Poshtekeshi Z, Haghparast A, Ghorbani M, Ranji H, Tavakoli M. Assessment of Neutron Contamination in Small Fields of Elekta Synergy Linac in High Energy Photon Beams. Iran J Med Phys 2026; 23 (3): 199-208. 10.22038/ijmp.2026.95945.2696.

## Introduction

Radiation therapy represents one of the most widely applied and effective approaches for managing solid tumors [1-3]. Its success, however, depends largely on the ability to deliver an adequate dose to the tumor while reducing exposure to surrounding healthy tissues [4, 5]. In contrast, conventional photon-based radiotherapy, commonly employed for treating deeply located tumors, presents its own limitations, including the generation of unwanted secondary radiation, particularly neutrons, which are not typically accounted for during treatment planning system [6, 7]. In an accelerator, high-energy electrons are either directly used for treatment of superficial tumors, or they impact a target and produce X-rays that are used for treatment of deep tumors [8]. Recently, the use of high-energy photons produced by medical linear accelerators, due to lower skin dose, higher dose in depth and lower scattered dose out of field, has become a common method for treatment of deep tumors of the body [9-11].

When linear accelerators work at energies above 10 MV, due to the collision of the photon beam with high-atomic materials such as lead and tungsten or their alloy that exist in the head of accelerator, a number of secondary radiations such as neutrons are produced, that are known as photoneutrons [12, 13]. Most of them are fast neutrons. Fast neutrons have radiological damages more than X-ray and scattered photons. In fact, neutrons are characterized by their relatively high linear energy transfer (LET), a property that increases their capacity to cause harmful biological effects in patients [3, 14-16]. Therefore, even a low radiation dose of neutrons can lead to biological effects, especially secondary malignancies [17-21]. These neutrons can reach to patient's body and lead to increasing patient dose, which is not measured in treatment planning process. Furthermore, penetration of fast neutrons is high, and they can penetrate in external shields and walls. As a result, they lead to unwanted dose to radiation workers and the public [18, 19, 22].

Few studies have been performed about neutron contamination in the photon mode of linear accelerators in small fields so far. Tajiki et al [23] used Monte Carlo simulation to evaluate neutron dose equivalent (NDE) at 18 MV energy with circular cones, assessing different field sizes and dose in locations on and off the central axis. Another study [24] employed

*Corresponding Author: Tel: +98 21 22439941; Fax: +98 21 22439941; E-mail: mhdghorbani@gmail.com

Monte Carlo simulation to study photoneutron production at 18 MV energy using circular cones of different sizes, emphasizing the need for precise neutron dose assessment in small fields. In these studies, doses were reported as relative quantities due to the simulation-based approach.

There are other studies that studied the contribution of neutron dose within or outside of the treatment field [25-28]. For example, Brkić et al [28], worked on the Monte Carlo simulation of linear accelerator photon beams and neutron contamination in the patient plane to check the neutron dose outside of treatment field. Lazem et al [25] compared the effect of field width on radiation dose within the treatment field. Ezzati and Studenski evaluated the patient dose from neutron contamination from several different field sizes at different depths [29] Jahangiri et al [30] investigated neutron contamination in an 18 MV Elekta linac and its dependence on field size. They indicated that neutron dose generally increases with larger field sizes. The study also found that neutron contamination outside the treatment field is not significantly influenced by field size. Biltekin et al [31] examined neutron doses in high-energy linacs and found that neutron dose at the field center increases with larger field sizes, especially beyond 10 × 10 $cm^2$.

In these studies, doses were reported as relative quantities due to the simulation-based approach. On the other hand, when adjusting the size of small fields, amount of high atomic number is increased in path of beam. Therefore, the present study was performed with the aim of measuring neutron contamination and absolute NDE in small fields for Elekta Synergy linac in high energy photon beam (10 MV and 18 MV) by using CR-39 detectors. Our study contributes to the neutron contamination and NDE in small radiation fields for the Elekta Synergy linac using high-energy photon beams (10 MV and 18 MV). Unlike earlier work which mostly used simulations and relative dose values, we used CR-39 detectors to measure these quantities directly and absolutely. We also explored how increasing materials with high atomic numbers in the beam path affects neutron production in these small fields. Our findings provide important practical data that can help improve treatment planning and safety in radiotherapy.

## Materials and Methods

CR-39 films (2 × 2 $cm^2$, 0.75 mm thick, TASLTRAK Ltd, Bristol, UK) were used to measure fast NDE. 45 film pieces for calibration and 192 film pieces for the measurement of neutron contamination. Films were chemically etched in 6.25 M NaOH solution at 85 °C for 3 hours, then analyzed under a light microscope (×40) to count neutron-induced tracks. Calibration was performed using a $^{241}$Am-Be neutron source with known doses (0.5-10 mSv), and a calibration curve was generated. For NDE measurements, CR-39 films were placed on and within an SP34 solid water phantom (Scanditronix-Welhofer, Germany) at surface and depth of maximum (2 cm for 10 MV, 2.5 cm for 18 MV) and irradiated using various field sizes (1 × 1 to 5 × 5 $cm^2$) on an Elekta Synergy linac.

CR-39 is a plastic polymer consists of short polyallyl chains that are linked by carbonate bonds and diethyleneglycol groups within a dense three-dimensional network, all connected through an initial monomer unit [32]. These films have a high potential for measuring the dose equivalent of fast neutrons in high-energy accelerators [30]. These films can measure only the NDE of fast neutrons because thermal neutrons cannot be tracked on CR-39 films [30]. When a charged particle impact with the film surface, as a result of its energy transfer, it creates a hidden track on the film surface, and this track is visualized by using chemical etching process [32, 33]. Neutrons cannot directly create any track on the film. However, because of neutron collision with the detectors, charged particles are produced, which can cause ionization and track on the CR-39 film. In general, the energy response range of CR-39 films depends on several parameters, such as the type of etching process (chemical or electrochemical), etching conditions (temperature, pressure, alkaline concentration, etc.), the composition of the base material used in CR-39 films, the background dose of these films, and so on [34, 35].

### *Calibration of CR-39 films*

The CR-39 detectors were calibrated at the Neutron Laboratory of the Atomic Energy Organization using a $^{241}$Am-Be neutron source. At the time of calibration, the source had an activity of 9.57 Ci (354 GBq) and a neutron emission rate of 1.949 × $10^7$ n/s. The source emits a continuous fast-neutron energy spectrum with average energy of approximately 4.5 MeV and maximum energy of about 11 MeV. A source-to-detector distance (SDD) of 50 cm was selected following previously reported CR-39 calibration procedures employing $^{241}$Am-Be neutron sources [36]. Although the CR-39 detector was calibrated using an $^{241}$Am-Be neutron source, the energy spectrum of photoneutrons generated by medical linear accelerators differs from that of the calibration source. Because the response of CR-39 detectors is energy dependent, this spectral mismatch may introduce uncertainty into the absolute NDE values. The potential impact of this limitation is discussed in the discussion section.

The calibration was performed in nine groups. In each calibration group, five CR-39 films were irradiated to target NDEs of 0.5, 1, 2, 3, 4, 5, 6, 8, and 10 mSv. Five additional unirradiated CR-39 detectors were used to determine the background track density, which was subtracted from that of the irradiated films. The resulting data were used to establish the calibration curve relating NDE to track density. No additional correction for possible photon-induced tracks was applied. The NDE was determined using the established CR-39 neutron dosimetry methodology, in which

neutron exposure is inferred predominantly from latent tracks produced by neutron-induced secondary charged particles. This methodology is consistent with previously published CR-39 neutron dosimetry studies performed using high-energy medical linear accelerators, where neutron dose measurements were reported without applying a separate photon-track correction [37–39].

During calibration, the irradiation time required to deliver each target NDE was calculated from the known NDE rate at the selected SDD after applying the corresponding scatter correction factor. The required exposure time was then obtained by dividing the target NDE by the corrected dose-equivalent rate.

***Chemical etching***

For optimal detection tracks, etching must be performed under standard conditions from the perspective of time of etching and temperature, concentration of alkaline material [40]. In this study, guidelines of the TASLTRAK Ltd company were followed for optimal chemical etching. In better words, chemical etching was performed for 3 h. The molar concentration of the NaOH was 6.25 M. The temperature of water bath in the Bain-Marie (Model WB 100, Shimi Fan, Iran) was 85 °C.

For chemical etching 1000 $cm^3$ of sodium hydroxide (NaOH) solution (EMPROVE®, Merck, Germany; Cat. No. 1.06482.1000) with molar concentration of 6.25 M was prepared. To make this solution, 250 g of NaOH powder (with a molar mass of 40 grams per mole) was needed, which was then dissolved in 1000 $cm^3$ of distilled water. After preparing the NaOH solution with the desired molar concentration, the solution was placed inside a Bain-Marie flask (Model WB 100, Shimi Fan, Iran) until its temperature reached 85 °C. When the thermometer (placed in NaOH solution) reached a temperature of 85 °C, the exposed films were placed in the solution for 3 h. After 3 h, the films were removed from Bain-Marie and washed with water. The films were then dried and prepared to count the tracks using a binocular light microscope (B1 Series, Motic, Hong Kong).

***Counting the tracks on the CR-39 films***

After completing chemical etching, the number of tracks on each film was counted using the optical microscope with magnification of ×40. Representative neutron tracks observed on the chemically etched CR-39 detector are shown in Figure 1. Before placing the films under the microscope for track counting, the microscope must be adjusted in a way that the number of tracks that are counted in a specific layer, be consistent across all films. This is important because slight variations in detector thickness may result in different numbers of visible tracks at different focal depths, potentially introducing variability in track counting.

To ensure that the same layer is being analyzed in all films, a tool known as a calibration slide was used. This slide has a series of circles with varying diameters. Depending on the magnification power of the objective lens being used, one of these circles was selected and placed under the microscope lens. The microscope was then adjusted using the microscope magnification screws until the selected circle comes into sharp focus. In this study, the circle with a diameter of 0.15 mm was used. Once this adjustment was made, the films were placed under the microscope for reading.

After microscope calibration, all CR-39 detectors were analyzed under identical optical conditions using the same focal plane and magnification. Track density was determined from ten microscopic fields of view for each detector, and the average value was used for dose calculation. Because all detectors had identical dimensions, underwent the same chemical etching procedure, and were analyzed using the same optical settings. This approach provided a consistent and reproducible basis for comparing NDE among the investigated irradiation conditions. Similar optical microscopy-based track counting procedures have been employed in previous CR-39 neutron dosimetry studies [37, 45, 46].

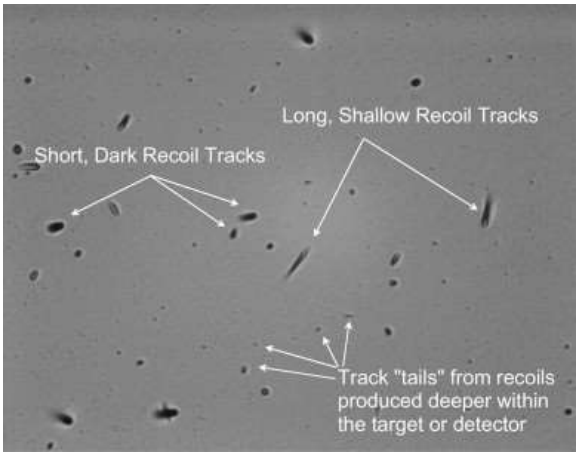



Figure 1. Neutron tracks observed on CR-39 detector after chemical etching, showing the damage trails left by fast neutrons. The tracks are viewed under a light microscope at × 40 magnification.

For each film, tracks were counted in 10 different fields of view. Figure 2 illustrates the distinction between true neutron tracks and background artifacts during image analysis. Real neutron tracks were distinguished from noise (e.g., scratches or alpha-particle tracks) based on their characteristic yellowish, bubble-like appearance. The average number of tracks counted in the ten fields of view was normalized to the microscope field-of-view area (0.0012 $cm^2$ at ×40 magnification) to obtain the track density (tracks/$cm^2$). Averaging the track counts from ten independent microscopic fields helped reducing the influence of local variations in track density and minimizing counting uncertainty. Finally, the NDE was calculated using the calibration equation and reported in mSv/Gy.

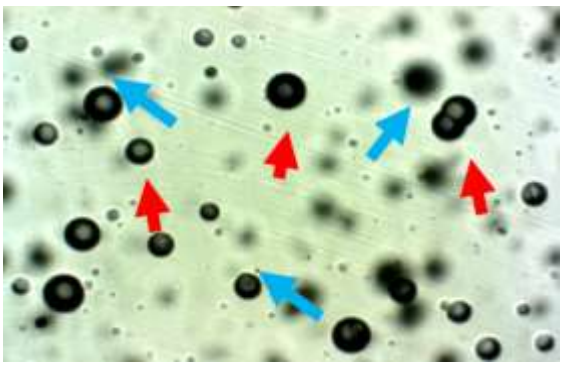


Figure 2. Optical microscope image showing real tracks (highlighted in red) and noise (highlighted in blue).

***NDE measurement setup***

A SP34 solid water phantom (Scanditronix-Welhofer, Germany) was used to simulate soft tissue equivalent conditions for measurement of NDE. It was made of sheets with dimensions of 30 × 30 $cm^2$ and thicknesses of 1, 2, 5 and 10 mm and consisted of RW3 polyester sheets. It included 1.2% titanium oxide ($TiO_2$) to match the scattering and stopping power of water. This phantom has special positions for placement of dosimeters. In this study, SP34 phantom was used to measure neutron contamination in terms of NDE at the depth of maximum dose. A schematic illustration of the experimental setup, including the irradiation geometry, phantom configuration, and the positions of the CR-39 detectors on the phantom surface and at the $d_{max}$, is presented in Figure 3.

In this study, an Elekta Synergy linac was used to expose the CR-39 films and neutron contamination for Elekta synergy linac was measured. For all exposures, the monitor unit was 200 MU and the source-surface distance (SSD) was 100 cm. The dimensions of the radiation fields were 1 × 1, 2 × 2, 3 × 3, 4 × 4, and 5 × 5 $cm^2$, which were arranged using collimator jaws (in the *y*-axis direction) and a multi-leaf collimator (MLC) (in the *x*-axis direction). The NDE was measured on the isocenter, which was aligned with the center of the field, and at the depth of maximum dose ($d_{max}$) in the phantom to obtain the dose inside the field. For obtaining the dose outside the field, measurements were done at off-axis distances of 5 cm and 10 cm from the field edges.

For each field at a specific energy level, irradiation at the surface of phantom was performed first, followed by depth irradiation, as follows. For measuring the fast NDE at the surface, for each field at a specific energy, five films were placed on the surface of the solid water phantom (one at the center of the field and the others at 5 cm and 10 cm from the field edges) and irradiated. Each measurement was repeated three times to ensure reproducibility.

To position the CR-39 detector at the depth of maximum dose ($d_{max}$), which is 2 cm for 10 MV photon beam energy, five 10 mm RW3 sheets of the SP34 solid water phantom were first stacked. This provided a base thickness of 5 cm. The CR-39 film was then placed on top of the fifth sheet, and two additional 10 mm sheets were placed above the film. This arrangement ensured that the detector was located precisely at 2 cm depth from the phantom surface while being surrounded by water-equivalent material, simulating realistic scattering and absorption conditions for accurate NDE measurement.

The same setup was repeated for 18 MV energy. The only difference was this point that the maximum depth dose at 18 MV is considered as 2.5 cm. In this case, five 10 mm RW3 sheets of the SP34 solid water phantom were first stacked. This provided a base thickness of 5 cm. Two 10 mm sheets and one 5 mm sheet were placed on the top of the film. Each irradiation condition was also repeated three times.

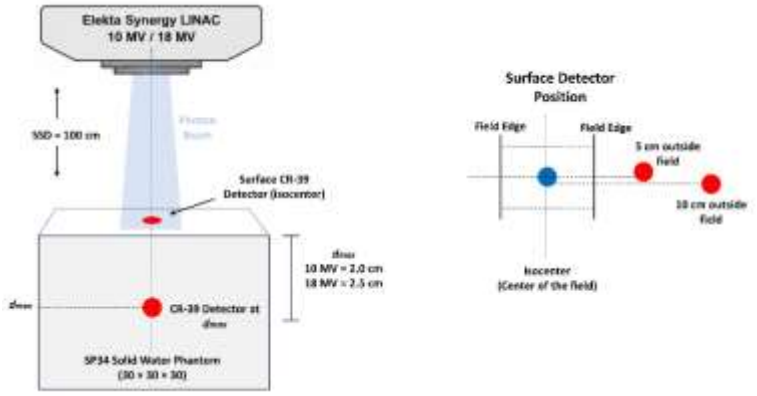



Figure 3. Schematic representation of the experimental setup used for NDE measurements (not to scale). CR-39 detectors were positioned on the phantom surface at the isocenter and at off-axis locations of 5 cm and 10 cm from the field edge, as well as at the $d_{max}$ inside the SP34 solid water phantom. Irradiations were performed using 10 MV and 18 MV photon beams with field sizes ranging from 1 × 1 to 5 × 5 $cm^2$, with SSD of 100 cm.

## Results

The results of the CR-39 detector calibration are presented in Figure 4. The calibration equation was empirically derived from the calibration measurements performed using the $^{241}$Am-Be neutron source. After background correction, the measured track densities corresponding to the known NDE values (0.5-10 mSv) were plotted to obtain the calibration curve. A second-order polynomial regression was then fitted to the experimental data, and the resulting equation was used to convert the measured track density (tracks/cm²) into NDE (mSv).

$$\text{Dose equivalent (mSv)} = 10^{-9}\,(\text{Track Density})^2 + 10^{-5}\,(\text{Track Density}) + 0.0589$$

where track density represents the number of tracks per cm².

The NDE at the center of the field on the phantom surface for different field sizes at 10 MV and 18 MV photon energy is shown in Figure 5. The results of the NDE measurements at the center of the field, at distances of 5 and 10 cm from the field edges for field sizes of 1 × 1, 2 × 2, 3 × 3, 4 × 4 and 5 × 5 cm² at two energies are presented in Table 1. It should be noted that in these tables, the 5 cm and 10 cm positions are along the longitudinal axis of the couch, directed toward the gantry or the patient's head.

Figure 6 compares the NDE measured at $d_{max}$ with that measured at the isocenter (center of the field) for the investigated field sizes at 10 MV and 18 MV photon energies.

Table 2 lists the percentage increase in NDE at the center of various field sizes compared to the center of the 5 × 5 cm² field at 10 MV and 18 MV energy.

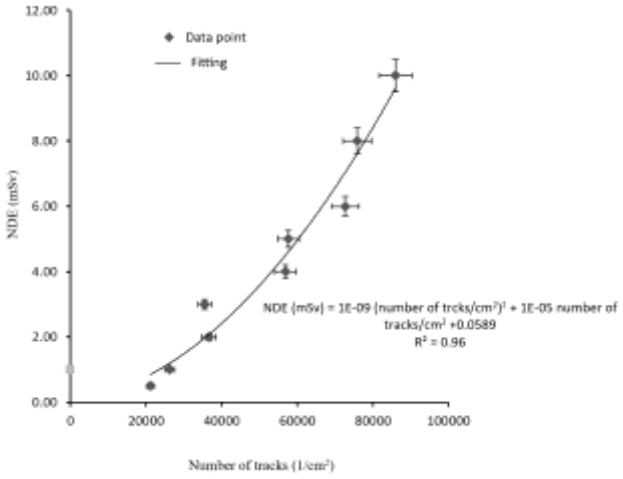



Figure 4. Calibration curve of CR-39 detectors: number of tracks (1/cm$^2$) versus NDE (mSv)

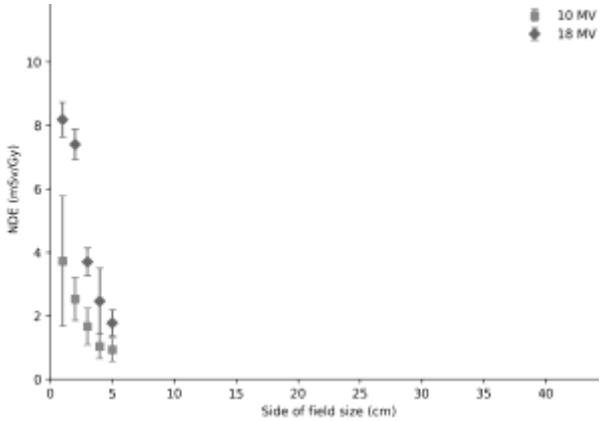



Figure 5. Comparison of NDE (mSv/Gy) at center of the field on the phantom surface for different field sizes in 10 MV and 18 MV photon energies

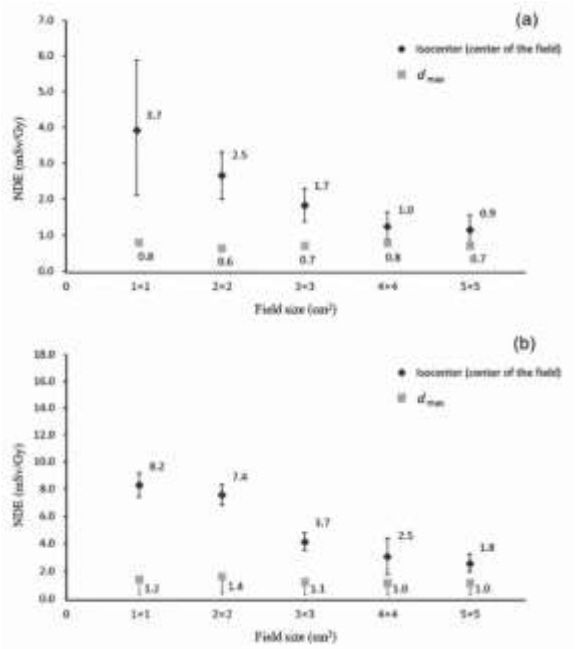



Figure 6. Comparison of NDE (mSv/Gy) at isocenter (center of the field) and dmax for different field sizes. a) dmax (2 cm) in 10 MV energy; (b) dmax (2.5 cm) in 18 MV energy

## Discussion

This study underscores how NDE impacts patient dose during high-energy photon radiotherapy. The obtained data indicates NDE is mainly influenced by field size (Figure 5), measurement location (in-field or out-of-field) (Table 1), and phantom depth (Figure 6). Highly contrary to expectation, smaller field sizes correlated to higher neutron doses. This pattern may result from neutron amplification by collimator system high-*Z* material interactions. Also, neutron contamination was highest near the irradiated field and decreased in depth, supporting the concept of neutron contamination being moderated and attenuated by tissue-equivalent material and phantom depth.

This study illustrates the pervasive gap in treatment planning systems (TPS) where neutron dose and related consequences are absent from dose calculations. Findings provide validation to work on neutron dose assessment and mitigations, more precisely in the high-energy small-field radiotherapy setting, and in alignment with the ALARA principle.

### *Clinical implications of NDE in high-energy radiotherapy*

The present study identified a maximum NDE of 8.18 mSv/Gy at 18 MV energy using the 1 × 1 cm² small field size. Although this value corresponds to a single treatment session, considering a typical treatment regimen of 25 to 30 sessions, the NDE could reach approximately 203.75 to 245.4 mSv/Gy. However, 8.18 mSv/Gy may appear minor, it is important to note that it corresponds to a relatively low MU setting of 200, which is typical of older 3D conformal radiotherapy techniques. Modern radiotherapy approaches, such as IMRT, often involve much higher MUs commonly 2 to 10 times greater [30] This increase in MU could lead to a proportional rise in neutron dose exposure.

These findings are supported by Kumar et al [47], who shown that patients undergoing high-energy (18 MV) radiotherapy can receive a measurable NDE both inside and outside the treatment field, which may be non-negligible depending on treatment geometry and shielding. Given that neutrons have a higher relative biological effectiveness (RBE) compared to photons and electrons, their contribution to potential late effects should not be ignored.

In line with the ALARA principle, it is crucial to minimize unnecessary neutron exposure, particularly when using small fields and high-energy photon beams. Current TPSs typically calculate dose distributions based on photon and electron components alone, potentially underestimating the total dose delivered to patients by neglecting neutron contamination contributions. Therefore, incorporating neutron dose evaluation into treatment planning is necessary to improve the accuracy of patient dose assessments and enhance radioprotection strategies.

### *Assessment of the impact of field size on NDE at the isocenter at $d_{max}$*

In this study, it was observed that the NDE decreased by increasing field size at the isocenter (center of the field) at both photon energies (Table 1). The highest NDE value (8.18 mSv/Gy) was recorded at the isocenter (center of the field) of the 1 × 1 cm² field with 18 MV energy, which was approximately five times greater than the value obtained for the 5 × 5 cm² field (1.77 mSv/Gy). The percentage increase in NDE for each field size relative to the 5 × 5 cm² field is summarized in Table 2, highlighting the progressive increase in neutron contamination as the field size decreases.

Table 1. NDE (mSv/Gy) measurement results at different distances and field sizes for 10 MV and 18 MV energy photons of Elekta Synergy linac

| Position | NDE (mSv/Gy) | | | | |
|---|---|---|---|---|---|
| | 1×1 cm² | 2×2 cm² | 3×3 cm² | 4×4 cm² | 5×5 cm² |
| 10 MV energy photons | | | | | |
| Center of Field (surface) | 3.72 ± 2.05 | 2.52 ± 0.68 | 1.66 ± 0.58 | 1.03 ± 0.39 | 0.93 ± 0.37 |
| 5 cm from field edge | 1.30 ± 0.95 | 0.65 ± 0.39 | 0.41 ± 0.07 | 0.42 ± 0.26 | 0.46 ± 0.13 |
| 10 cm from field edge | 0.56 ± 0.19 | 0.45 ± 0.06 | 0.39 ± 0.10 | 0.34 ± 0.14 | 0.34 ± 0.01 |
| 18 MV energy photons | | | | | |
| Center of Field (surface) | 8.18 ± 0.55 | 7.40 ± 0.48 | 3.69 ± 0.44 | 2.46 ± 1.04 | 1.77 ± 0.41 |
| 5 cm from field edge | 0.52 ± 0.36 | 0.74 ± 0.28 | 0.69 ± 0.42 | 0.96 ± 0.59 | 0.49 ± 0.17 |
| 10 cm from field edge | 0.78 ± 0.08 | 0.62 ± 0.38 | 0.43 ± 0.19 | 0.57 ± 0.26 | 0.36 ± 0.08 |

Table 2. Percentage increase in NDE at the field center relative to the 5 × 5 cm² field for 10 MV and 18 MV photon beams.

| Dose change (%) | Reference field size (cm²) | Compared field size (cm²) |
|---|---|---|
| | 10 MV photon energy | |
| 300.00 % | 5×5 (0.93) | 1×1 (3.72) |
| 170.90 % | 5×5 | 2×2 (2.52) |
| 78.40 % | 5×5 | 3×3 (1.66) |
| 10.70 % | 5×5 | 4×4 (1.03) |
| | 18 MV photon energy | |
| 362.10 % | 5×5 (1.77) | 1×1 (8.18) |
| 318.10 % | 5×5 | 2×2 (7.40) |
| 108.40 % | 5×5 | 3×3 (3.69) |
| 38.90 % | 5×5 | 4×4 (2.46) |

One possible explanation for this trend is the increased contribution of photoneutron production in the beam-defining components under very small-field conditions. As the field size decreases, especially in small-field conditions (≤ 5 × 5 cm²), the jaws and MLCs are positioned closer together, leading to more high-Z elements (e.g., tungsten, lead) being present in the beam path, which in turn increases the photoneutron production. In contrast, Jahangiri et al. [30] reported an overall increase in NDE with increasing field size, while emphasizing that this relationship was not linear and depended on the degree of collimator opening. Their study investigated field sizes ranging from 5 × 5 to 30 × 30 cm², whereas the present study focused exclusively on small fields (1 × 1 to 5 × 5 cm²). Therefore, the apparent discrepancy may reflect differences in the investigated field-size range as well as variations in accelerator design, beam-defining components, and experimental conditions. These findings indicate that the dependence of photoneutron contamination on field size is not universal but is influenced by irradiation geometry, particularly in small-field radiotherapy.

As shown in Figure 6 for a given photon energy, the amounts of NDE in $d_{max}$ for different field sizes are close to each other. In other words, the results obtained were independent of the field size. It means that at a constant depth ($d_{max}$), there was no significant relationship between changes in field size and NDE. Since CR-39 detectors are sensitive only to fast neutrons, the measurements at $d_{max}$ represent only the fast-neutron component because thermal neutrons cannot be registered by the detector. Furthermore, the CR-39 detector was calibrated using an $^{241}$Am-Be neutron source, whereas the energy spectrum of photoneutrons generated by medical linear accelerators differs from that of the calibration source. Because the response of CR-39 is energy dependent, this spectral mismatch may introduce additional uncertainty into the absolute NDE values. Nevertheless, the detector remains sensitive over the fast-neutron energy range, allowing meaningful relative comparisons among the investigated irradiation conditions. Therefore, the quantitative results should be interpreted with consideration of this energy-dependent response. Another limitation of the present methodology is that no separate correction was applied for photon-induced tracks within the CR-39 detector material. However, the NDE was determined using the established CR-39 neutron dosimetry methodology, in which the detector response is attributed predominantly to neutron-induced secondary charged particles. This approach has been widely adopted in previous CR-39 neutron dosimetry studies performed with high-energy medical linear accelerators and allows consistent relative comparison of NDE among the investigated irradiation conditions [37-39]. Nevertheless, any potential contribution from photon-induced reactions cannot be completely excluded and should be considered when interpreting the absolute values of the measured NDE. Under these conditions, no significant relationship was observed between field size and the

measured fast-neutron NDE at $d_{max}$. While field size influences NDE near the phantom surface through interactions in the secondary collimators and other high-Z beam-defining components, this effect becomes less pronounced at greater depths, where neutron scattering, moderation, and absorption dominate.

Other studies such as Israngkul-Na-Ayuthaya et al [41] assessed neutron and activation product doses from a 15 MV linac, while Hashemi et al [42] investigated photoneutron production from wedge filters. However, none of these studies explored neutron dose variation in small fields ($\leq 5 \times 5$ cm$^2$), which are increasingly used in modern radiotherapy techniques such as stereotactic radiosurgery. Therefore, the contrast between the results of the present study and those of earlier investigations lies in the range of field sizes examined. While previous studies focused primarily on standard or large fields, the present work emphasizes the increased neutron contamination dose in small-field settings, providing important implications for neutron shielding and secondary cancer risk in high-precision radiotherapy.

***Assessment of the NDE at center of the field and out of field***

Based on our findings for each field size and energy, the NDE measured at the distance of 10 cm from the field edge was lower than that measured at the field center and at 5 cm from the field edge. Higher NDE near the isocenter (center of the field) was observed (Table 1). Two main factors can explain this observation. First, most of the neutrons generated in high-energy linear accelerators are fast neutrons [43]. Due to their high energy and low scattering cross-section, these neutrons primarily propagate in forward directions and tend to accumulate near the field center, resulting in higher NDE values there [44]. As the distance from the field center increases, fewer neutrons reach a higher distance from the field center at those points, leading to a reduced dose. Second, the energy of photoneutrons depends on the type of material involved in the photonuclear interaction. For example, when high-energy photons interact with components made of steel or iron in the primary collimator and flattening filter, neutrons with relatively higher energies are produced. In contrast, interactions with tungsten, which is used in secondary collimators in MLCs and jaws, typically yield neutrons with lower energies [27].

These differences in neutron energy affect how far they can travel. High energy neutrons generated in the upper parts of a linac have greater penetration ability and are more likely to reach the central region of the treatment field. In comparison, lower energy neutrons produced in the lower parts of the linac near the field edge are less penetrating and lose their energy more rapidly. As a result, their contribution to the NDE diminishes with increasing distance from the field center. This explains the observed decrease in NDE at off-axis positions compared to the center of the field. Previous studies [18, 28, 29] did not report a significant correlation between NDE and distance from the field center on the phantom surface. However, they consistently showed that, for a fixed field size, the NDE decreases with increasing distance from the field center.

***Assessment of the NDE in $d_{max}$ and isocenter (center of the field)***

According to the results, for all field sizes examined at both 10 MV and 18 MV energies, the NDE at the depth of maximum dose ($d_{max}$) inside the phantom was significantly lower than the corresponding value measured at the isocenter (center of the field) (Figure 6). Several factors may contribute to this observation. Photoneutrons produced in the head of a medical linear accelerator are predominantly fast neutrons [45]. As these neutrons traverse the phantom, they undergo repeated elastic scattering interactions with light nuclei, progressively transferring part of their kinetic energy to the surrounding medium. Consequently, their energy progressively decreases with depth through neutron moderation, and a fraction of the fast neutrons eventually reaches the thermal energy range. This reduction in energy, together with changes in neutron fluence, contributes to a decrease in the measured fast-neutron NDE with increasing depth. However, this observation should be interpreted with caution because CR-39 detectors are primarily sensitive to fast neutrons and exhibit little or no response to thermal neutrons. Therefore, part of the observed reduction in NDE at greater depths may reflect the reduced sensitivity of the detector to thermalized neutrons rather than a complete reduction in the actual NDE.

A similar depth-dependent trend was reported by Thekkedath et al [46], who found that photoneutron dose decreased as depth increased under various irradiation geometries using passive neutron detectors. Likewise, Khajetash et al [37] observed that fast neutron contamination was significantly higher near the phantom surface, especially in the presence of wedges, and diminished with increasing depth. Additionally, Kumar et al [47], in their optimization study of CR-39 detectors for neutron contamination dosimetry using a $^{252}$Cf neutron source, emphasized the importance of depth correction factors, particularly due to the reduced energy and fluence of neutrons detected at deeper phantom layers. Overall, these studies support the depth-dependent trend observed in the present work. Nevertheless, because CR-39 detectors primarily measure the fast-neutron component, the decrease in NDE observed at greater depths should not be interpreted solely as a reduction in the total NDE. Rather, it may also reflect the progressive thermalization of neutrons within the phantom and the limited sensitivity of CR-39 detectors to thermal neutrons.

## Conclusion

This research highlights important factors influencing the NDE in high-energy photon radiotherapy. The results indicated that for 18MV photon energy, NDE was greater in smaller field geometries owing to the increased production of

photoneutrons in the high-Z components of the linear accelerator head. Furthermore, NDE decreased significantly as the distance away from the center of the field increased and as depth into the phantom increased, which indicates the directionality and energy dependence of the photoneutron field. Interestingly, the NDE's steady values at $d_{max}$ with changing field sizes combined with the detector's energy dependence, indicates depth was a greater factor than field size in determining neutron dose distributions. It is also important not to trivialize the contribution of neutrons because of the increased RBE of neutrons, in addition to their potentially prolonged biological effects.

These results promote the incorporation of neutron contamination dosimetry into the treatment planning procedure in small fields, particularly where techniques utilize high energy photons in small fields (e.g., IMRT and stereotactic radiosurgery), to further enhance radiological protection and promote an expanded risk assessment consistent with ALARA in modern radiotherapy.

## Acknowledgment

The authors appreciate Kermanshah university of Medical Sciences for financial support of this study.

## References

1. Barton MB, Frommer M, Shafiq J. Role of radiotherapy in cancer control in low-income and middle-income countries. Lancet Oncol. 2006;7(7):584–95.
2. De Ruysscher D, Niedermann G, Burnet NG, Siva S, Lee AW, Hegi-Johnson F. Radiotherapy toxicity. Nat Rev Dis Primers. 2019;5(1):13.
3. Assalmi M, Diaf EY. The behavior of the contamination particles appears with the 18 MV photon beam delivered by Elekta Synergy MLCi2. Radiat Phys Chem. 2022;199:110384.
4. Chen HH, Kuo MT. Improving radiotherapy in cancer treatment: Promises and challenges. Oncotarget. 2017;8(37):62742.
5. Schaue D, McBride WH. Opportunities and challenges of radiotherapy for treating cancer. Nat Rev Clin Oncol. 2015;12(9):527–40.
6. Moghaddam FF, Bakhshandeh M, Ghorbani M, Mofid B. Assessing the out-of-field dose calculation accuracy by Eclipse treatment planning system in sliding window IMRT of prostate cancer patients. Comput Biol Med. 2020;127:104052.
7. Van Hoey O, Stolarczyk L, Lillhök J, Eliasson L, Mojzeszek N, Liszka M, et al. Simulation and experimental verification of ambient neutron doses in a pencil beam scanning proton therapy room as a function of treatment plan parameters. Front Oncol. 2022;12:903537.
8. Khan FM. The physics of radiation therapy. 2nd ed. Lippincott Williams & Wilkins; 2009. p. 779–88.
9. Rudd P, Prior D, Austin-Smith S. Neutron contamination of 10 MV X-rays: its relevance to treatment room door and maze design. Br J Radiol. 2007;80(954):469–75.
10. Mesbahi A, Ghiasi H, Mahdavi SR. Photoneutron and capture gamma dose equivalent for different room and maze layouts in radiation therapy. Radiat Prot Dosimetry. 2010;140(3):242–9.
11. Hashemi F, Hashemi-Malayeri B, Raisali G, Shokrani P, Sharafi A. A study of the photoneutron dose equivalent resulting from a Saturne 20 medical linac using Monte Carlo method. Nukleonika. 2007;52(1):39–43.
12. NCRP. NCRP Report No. 93: Ionizing Radiation Exposure of the Population of the United States. Bethesda, MD: National Council on Radiation Protection and Measurements; 1993.
13. Olsen KJ. Neutron contamination from medical electron accelerators (NCRP Report No. 79). Bethesda, MD: National Council on Radiation Protection and Measurements; 1986.
14. Elmtalab S, Shanei A, Choopan Dastjerdi MH, Brkić H, Abedi I, Amouheidari A. Determination of the neutron contamination during brain radiotherapy using a moderated-boron trifluoride detector and the MCNP Monte Carlo code. Radiat Prot Dosimetry. 2022;198(3):129–38.
15. Shojaei M, Rashedi S, Chakoli AN, Karimi AH, Geraily G. Measurement of neutron equivalent dose in the thyroid, chiasma, and lens for patients undergoing pelvic radiotherapy: A phantom study. Appl Radiat Isot. 2022;184:110188.
16. Banaee N, Goodarzi K, Nedaie HA. Neutron contamination in radiotherapy processes: a review study. J Radiat Res. 2021;62(6):947–54.
17. Vega-Carrillo H, Ortíz-Hernandez A, Hernandez-Davila V, Hernández-Almaraz B, Montalvo T. H*(10) and neutron spectra around linacs. J Radioanal Nucl Chem. 2010;283(2):537–40.
18. ICRP. ICRP Publication 103: The 2007 Recommendations of the International Commission on Radiological Protection. Ann ICRP. 2007;37(2-4):1-332.
19. Xu XG, Bednarz B, Paganetti H. A review of dosimetry studies on external-beam radiation treatment with respect to second cancer induction. Phys Med Biol. 2008;53(13):R193.
20. Alfuraih A, Chin M, Spyrou N. Measurements of the photonuclear neutron yield of 15 MV medical linear accelerator. J Radioanal Nucl Chem. 2008;278:681–4.
21. Ongaro C, Zanini A, Nastasi U, Ródenas J, Ottaviano G, Manfredotti C. Analysis of photoneutron spectra produced in medical accelerators. Phys Med Biol. 2000;45(12):L55.
22. Newhauser WD, Durante M. Assessing the risk of second malignancies after modern radiotherapy. Nat Rev Cancer. 2011;11(6):438–48.
23. Tajiki S, Nedaie HA, Rahmani F. A Monte Carlo study of neutron contamination in presence of circular cones during stereotactic radiotherapy with 18 MV photon beams. Biomed Phys Eng Express. 2020;6(3):035016.
24. Hosseinzadeh E, Banaee N, Nedaie HA. Monte Carlo calculation of photo-neutron dose produced by circular cones at 18 MV photon beams. Rep Pract Oncol Radiother. 2018;23(1):39–46.

25. Lazem BS, Hassan IJ, Rejah BK, Khalaf H, Mostafa MYA. Field Width Comparison of the Photon Beams 6 MV and 10 MV Coming Out of the Radiotherapy Linear Accelerator. Baghdad Sci J. 2025;22(7):2313–20.
26. Gabrisch L, Cecchetto M, Delfs B, Looe HK, Budroweit J, Alía RG, et al. Quantification of neutron-induced single event upsets in a static random-access memory by clinical high-energy photon beam. IEEE Trans Nucl Sci. 2024;71(3):1-7.
27. Assalmi M, Alshreef A, Diaf EY, Arectout A, Ade N, El Berhdadi EH. Quantitative Assessment of Photoneutron-induced Secondary Radiation Dose in Prostate Treatment Using an 18 MV Medical Linear Accelerator: A Monte Carlo Study. J Med Phys. 2024;49(4):673–86.
28. Brkić H, Ivković A, Kasabašić M, Sovilj MP, Jurković S, Štimac D, et al. The influence of field size and off-axis distance on photoneutron spectra of the 18 MV Siemens Oncor linear accelerator beam. Radiat Meas. 2016;93:28–34.
29. Ezzati AO, Studenski MT. Neutron damage induced in cardiovascular implantable electronic devices from a clinical 18 MV photon beam: a Monte Carlo study. Med Phys. 2017;44(11):5660–6.
30. Jahangiri M, Hejazi P, Hashemi SM, Haghparast A, Hajizadeh B. The effect of field size and distance from the field center on neutron contamination in medical linear accelerator. Int J Adv Biol Biomed Res. 2015;3(1):97–104.
31. Biltekin F, Yeginer M, Ozyigit G. Investigating in-field and out-of-field neutron contamination in high-energy medical linear accelerators based on the treatment factors of field size, depth, beam modifiers, and beam type. Phys Med. 2015;31(5):517–23.
32. Jaffray DA, Gospodarowicz MK. Radiation therapy for cancer. In: Gelband H, Jha P, Sankaranarayanan R, Horton S, editors. Cancer: Disease Control Priorities, 3rd edition, Volume 3. Washington (DC): The International Bank for Reconstruction and Development/The World Bank; 2015.
33. Negi A, Semwal A, Chandra S, Hariwal R, Sonkawade R, Kanjilal D, et al. Modifications induced by Li+3, Ni+9 and Au+9 ion beams to CR-39 polymer track detector. Radiat Meas. 2011;46(1):127–32.
34. Nedaie HA, Darestani H, Banaee N, Shagholi N, Mohammadi K, Shahvar A, et al. Neutron dose measurements of Varian and Elekta linacs by TLD600 and TLD700 dosimeters and comparison with MCNP calculations. J Med Phys. 2014;39(1):10–7.
35. Sohrabi M, Hakimi A. Fast, epithermal and thermal photoneutron dosimetry in air and in tissue equivalent phantom for a high-energy X-ray medical accelerator. Z Med Phys. 2018;28(1):49–62.
36. Bogard JS, Golzarri JI, Espinosa G. Dose calibration and track diameter distribution for 241Am-Be neutron source, using CR-39 nuclear track methodology. J Nucl Phys Mater Sci Radiat Appl. 2018;6(1):77–80.
37. Khajetash B, Toossi MTB, Ghorbani M, Jahangiri M, Akbari F. Measurement of fast neutron contamination caused by the presence of wedge and block using CR-39 detector. J Cancer Res Ther. 2019;15(Suppl 1):S103–9.
38. Fujibuchi T, Kodaira S, Sawaguchi F, Abe Y, Obara S, Yamaguchi M, et al. Measurement of the secondary neutron dose distribution from the LET spectrum of recoils using the CR-39 plastic nuclear track detector in 10 MV X-ray medical radiation fields. Nucl Instrum Methods Phys Res B. 2015;349:239–45.
39. Mohammadi S, Behmadi M, Mohammadi A, Bahreyni Toossi MT. Thermal and fast neutron dose equivalent distribution measurement of 15-MV linear accelerator using CR-39 nuclear track detectors. Radiat Prot Dosimetry. 2020;188(4):503–7.
40. Fleisher R, Price P, Walker R. Nuclear tracks in solids: Principles and applications. Berkeley; 1975.
41. Israngkul-Na-Ayuthaya I, Suriyapee S, Pengvanich P. Evaluation of equivalent dose from neutrons and activation products from a 15-MV X-ray LINAC. J Radiat Res. 2015;56(6):919–26.
42. Hashemi SM, Hashemi-Malayeri B, Raisali G, Shokrani P, Sharafi AA, Torkzadeh F. Measurement of photoneutron dose produced by wedge filters of a high energy linac using polycarbonate films. J Radiat Res. 2008;49(3):279–83.
43. Kry SF, Howell RM, Salehpour M, Followill DS. Neutron spectra and dose equivalents calculated in tissue for high-energy radiation therapy. Med Phys. 2009;36(4):1244–50.
44. Li D, Deng X, Xue Y, Lou Z, Zhang Y, Guo W, et al. Neutron dose distribution in the treatment room for an accelerator in the flattening filter-free mode. Precis Radiat Oncol. 2017;1(1):13–9.
45. Kim HS, Park YH, Koo BC, Kwon JW, Lee JS, Choi HS. Evaluation of the photoneutron field produced in a medical linear accelerator. Radiat Prot Dosimetry. 2007;123(3):323–8.
46. Thekkedath SC, Raman RG, Musthafa M, Bakshi A, Pal R, Dawn S, et al. Study on the measurement of photo-neutron for 15 MV photon beam from medical linear accelerator under different irradiation geometries using passive detectors. J Cancer Res Ther. 2016;12(2):1060–4.
47. Kumar V, Sonkawade RG, Dhaliwal AS. Optimization of CR-39 as neutron dosimeter. Indian J Pure Appl Phys. 2010;48(7):466-469